

## 1 *Single shot detector application for image disease localization*

2

3 **Authors:** Rushikesh Chopade<sup>1</sup>, Aditya Stanam<sup>2</sup>, & Shrikant Pawar<sup>3\*</sup>

4 **Addresses:** <sup>1</sup>Department of Geology & Geophysics, Indian Institute of Technology, Kharagpur,  
5 India. <sup>2</sup>Department of Toxicology, University of Iowa, Iowa City, Iowa 52242-5000, USA. <sup>3</sup>Yale  
6 Center for Genomic Analysis, Yale School of Medicine, Yale University, New Haven,  
7 Connecticut, 30303, USA.

8 **Correspondence:** \*Shrikant Pawar, E-mail: [shrikant.pawar@yale.edu](mailto:shrikant.pawar@yale.edu), Phone: +001-404-431-  
9 0213

10 **Authors:** Aditya Stanam, E-mail: [aditya-stanam@uiowa.edu](mailto:aditya-stanam@uiowa.edu), Rushikesh Chopade, E-mail:  
11 [rushikeshchopaderc@gmail.com](mailto:rushikeshchopaderc@gmail.com)

12

### 13 **Abstract:**

14 Bounding box algorithms are useful in localization of image patterns. Recently, utilization  
15 of convolutional neural networks on X-ray images has proven a promising disease prediction  
16 technique. However, pattern localization over prediction has always been a challenging task with  
17 inconsistent coordinates, sizes, resolution and capture positions of an image. Several model  
18 architectures like Fast R-CNN, Faster R-CNN, Histogram of Oriented Gradients (HOG), You only  
19 look once (YOLO), Region-based Convolutional Neural Networks (R-CNN), Region-based Fully  
20 Convolutional Networks (R-FCN), Single Shot Detector (SSD), etc. are used for object detection  
21 and localization in modern-day computer vision applications. SSD and region-based detectors like  
22 Fast R-CNN or Faster R-CNN are very similar in design and implementation, but SSD have shown  
23 to work efficiently with larger frames per second (FPS) and lower resolution images. In this article,  
24 we present a unique approach of SSD with a VGG-16 network as a backbone for feature detection  
25 of bounding box algorithm to predict the location of an anomaly within chest X-ray image.

26 **Keywords:** Convolutional Neural Networks; Single Shot Detector  
27 Word count, Abstract: 163

28 **Word count, Body of manuscript:** 1109

29 **Running Head:** *Image disease localization with single shot detector*

30

### 31 **Introduction:**

32 Object localization is a subfield of computer vision that is used to detect the location of  
33 object in an image. Several model architectures like Fast R-CNN [1], Faster R-CNN [2], Histogram  
34 of Oriented Gradients (HOG) [3], You only look once (YOLO) [4], Region-based Convolutional  
35 Neural Networks (R-CNN) [5], Region-based Fully Convolutional Networks (R-FCN) [6], Single  
36 Shot Detector (SSD) [7] and Spatial Pyramid Pooling (SSP-net) [8] are been used for object  
37 detection and localization in modern-day computer vision applications. The SSD and region-based  
38 detectors like Fast R-CNN or Faster R-CNN are very similar in design and implementation, but  
39 SSD have shown to work efficiently with larger frames per second (FPS) and lower resolution

40 images [7]. Although Region-based detectors like Faster R-CNN have a little greater accuracy as  
41 compared to SSD, SSD's are faster and better for real-time image processing [9]. Thus, we present  
42 a unique approach of SSD with a VGG-16 network as a backbone for feature detection of bounding  
43 box algorithm to predict the location of an anomaly within chest X-ray image.

44

## 45 **Method:**

46

### 47 **1) Data collection:**

48 The image dataset for developing bounding box algorithms has been retrieved from  
49 National Institutes of Health (NIH) kaggle portal. The dataset consists of 112,120 chest X-ray  
50 images, each image with a 1024\*1024-pixel resolution. The images are divided into 15 classes  
51 ('No Finding', 'Atelectasis', 'Cardiomegaly', 'Consolidation', 'Effusion', 'Emphysema', 'Edema',  
52 'Fibrosis', 'Infiltration', 'Mass', 'Nodule', 'Pneumonia', 'Pneumothorax', 'Pleural Thickening' and  
53 'Hernia'). Further, each X-ray image consists of information on 4 bounding box attributes which  
54 bound the exact location of the detected disease. The first coordinate (x\_min) marks the x  
55 coordinate of the top left corner of the bounding box which can be considered as the origin with  
56 pixels measured from this corner of the image. Similarly, the second attribute (y\_min) marks the  
57 y coordinate of the top left corner of the bounding box. The remaining two attributes are the width  
58 and height of the bounding box in unit pixels length. Figure 1 is the X-ray image of a patient  
59 suffering from cardiomegaly. The red bounding box shows the location of the infection in the  
60 image. The image is downscaled to 512\*512 from 1024\*1024, 1024\*1024 being the original  
61 resolution of X-ray image. The top left corner of the image (0,0) is taken as the origin with x\_min  
62 and y\_min as the x and y coordinates of bounding boxes.

63

64 *Figure 1: Depicts the location of cardiomegaly with bounding boxes.*

65

### 66 **2) Exploratory data analysis and preprocessing:**

67 For training, the width and height attributes were converted to x\_max and y\_max by adding  
68 the width attribute of the bounding box to the corresponding x\_min coordinate for obtaining x\_max  
69 and by adding the height attribute to the y\_min for obtaining y\_max coordinate. Thus, the bounding  
70 box coordinates can now be presented with a string containing x\_min, y\_min, x\_max, and y\_max  
71 coordinates. The images with multiple labels (93) would create a situation of high bias and abide  
72 the algorithm from learning the location of the disease with precision. Therefore, the images with  
73 multiple labels have not been included in training the algorithms. In total, 787 images with single  
74 labels have only been considered for training. The plot for the top 15 labels (single + multiple) has  
75 been shown in figure 2.

76

77 *Figure 2: The plot for the top 15 labels.*

78

79 Dynamic training has been implemented to reduce the computational cost with weights updated  
80 by backpropagation for every 4 images. An image data generator class has been utilized for this  
81 technique.

82

83 *Table 1: Number of training batches, sizes, and input pixel resolution for bounding box algorithms.*

84

### 85 **3) Network architecture:**

86 Several factors can impact the accuracy and training speed of algorithm, some can be  
87 feature extractors (VGG-16, InceptionNet, ResNet, MobileNet, etc.), input image resolutions,  
88 matching strategy and IOU threshold, non-max suppression IOU threshold, number of predictions,  
89 boundary box encoding, data augmentation, size of training dataset, use of multi-scale images in  
90 training and testing, training configurations including batch size, input image resize, learning rate,  
91 learning rate decay and localization loss function [9]. An SSD runs a convolutional network on  
92 input image and computes a feature map, it then runs  $n*n$  convolutional kernels on this feature  
93 map to predict the bounding boxes and categorization probability [10]. For this SSD model, a  
94 VGG-16 feature extractor has been used with pretrained ImageNet weights with an input size of  
95  $512*512*3$  resolution. The reason for using a feature extractor was to get the features of objects  
96 in specific order, which eventually would help the algorithm learn faster. VGG-16 feature extractor  
97 is followed by rectified linear activation layer, followed by a dropout layer to construct algorithms  
98 backbone. A dropout layer with 25% dropout nodes has been used to address the high variance  
99 problem. The output image after the dropout layer application has a dimension of  $16*16*512$   
100 resolution. After the dropout layer, compression layers are added to the model architecture,  
101 containing a 2D convolutional layer, a ReLU activation layer, and a batch normalization layer. The  
102 detailed structure of this compression layer is shown in figure 3. The first compression layer has a  
103 convolutional layer of kernel size 3, a stride of 1, number of filters as 256. The output shape is  
104 obtained by the following formula:

105

$$106 \text{ Output Dimension} = ((\text{Input Dimension} + 2p - f)/s) + 1$$

107

108 Where, “ $p$ ” is padding, “ $f$ ” is kernel size, and “ $s$ ” is the stride used in layer. For convolutional layer  
109 of the first compression layer, with  $p=1$ ,  $f=3$ , and  $s=1$  generates an output shape  $16*16*256$

110 resolution. The second compression layer with  $p=1$ ,  $f=3$ ,  $s=1$  and number of filters=128, generates  
111 an output shape of  $8*8*128$ , this is followed by the last compression layer. After 3 compression  
112 layers, the model splits into 2 branches, classification branch and a bounding box regression branch.  
113 The classification branch classifies the image into the classes from the given labels. The 2D  
114 convolutional layer is followed by an activation layer containing the sigmoid activation function,  
115 followed by a flattening layer. The final output shape of the classification branch after flattening  
116 is equal to 16. With similar approach on bounding box regression branch, the final output shape  
117 of the classification branch after flattening equals to 64. The flattened layers of the classification  
118 and bounding box regression branches are concatenated to get final output shape with 16 bounding  
119 box predictions. The non-max suppression technique is applied to generate a single confidence  
120 value.

121

#### 122 **4) Custom cost function:**

123 The compression layer has been designed to increase the number of filters/channels. The  
124 2D convolutional layer is followed by a rectified linear (ReLU) activation function. The ReLU is  
125 followed by a Batch normalization layer, which helps to stabilize the learning process and  
126 dramatically reduces the number of training epochs required to train the network. A 0.25 fraction  
127 dropout regularization has been applied to the model in order to reduce the degree of overfitting,  
128 25% of the random nodes have been dropped with remaining nodes as input for the next hidden  
129 layer. The final SSD model after concatenation requires an additional custom loss function for  
130 training.

131

132 *Figure 3: The SSD model architecture.*

133

134 *Figure 4: Compression layer architecture used in SSD model.*

135

136 A custom cost function has been used to minimize the loss while training SSD algorithm. The cost  
137 function has two parts. One-part deals with classification loss while the other part deals with  
138 bounding box loss. This bounding box loss part of the custom cost function is based on intersection  
139 over union policy. In figure 5, the predicted bounding box of a patient suffering from cardiomegaly  
140 is shown in blue color. The original bounding box presenting the ground truth is shown in red  
141 color. The region of intersection of the two bounding boxes is shown in green color. The union of  
142 the two bounding boxes is simply the total area occupied by both the bounding boxes. The  
143 intersection over union is defined as area of region of intersection divided by the area of the region  
144 of union. The more is the intersection over union for the image, the lesser is the training loss. This  
145 custom cost function works to decrease the loss by increasing the area of overlap for two bounding  
146 boxes.

147

148 *Figure 5: Image of a patient suffering from cardiomegaly showing intersection over union policy*  
149 *for the custom cost function.*

150

151 *Figure 6: Comparison of ground truth with bounding box predicted with SSD Model.*

152

### 153 **Results and Discussion:**

154 The predicted bounding box is found to provide an accurate position of the disease  
155 (cardiomegaly). The region of prediction is observed to be larger than that of the actual bounding  
156 box (figures 5 & 6). Although the region of bounding box was bigger than the actual ground truth  
157 bounding box, it seemed a reasonable offset. Further, training with additional images is likely to  
158 improve the box prediction score.

159

160 *Table 2: Number of training epochs and losses for all algorithms.*

161

162 This seems a promising strategy of utilizing SSD with a VGG-16 network as a backbone for feature  
163 detection of bounding box algorithm to predict the location on X-ray images. Its applications  
164 should be tested on other medical image datasets like computerized tomography, magnetic  
165 resonance image or even immunohistochemistry staining images. Bounding boxes are one of the  
166 most popular image annotation techniques in deep learning, and with improvements in prediction  
167 accuracies, this method can reduce costs and increase annotation efficiency compared to other  
168 image processing methods.

169

### 170 **Supplementary data:**

171 1) National Institute of Health chest X-ray dataset: <https://www.kaggle.com/nih-chest-xrays/data>

172 2) Bounding box coordinates of the testing images: [https://www.kaggle.com/nih-chest-](https://www.kaggle.com/nih-chest-xrays/data?select=BBox_List_2017.csv)  
173 [xrays/data?select=BBox\\_List\\_2017.csv](https://www.kaggle.com/nih-chest-xrays/data?select=BBox_List_2017.csv)

174 3) Analysis code can be retrieved from here:  
175 [https://bitbucket.org/chestai/chestai\\_rushikes\\_code/src/master/](https://bitbucket.org/chestai/chestai_rushikes_code/src/master/)

176

177 **Author contributions:**

178 SP, AS, and RC conceived the concepts, planned, and designed the article. SP, AS, and RC  
179 primarily wrote and edited the manuscript.

180

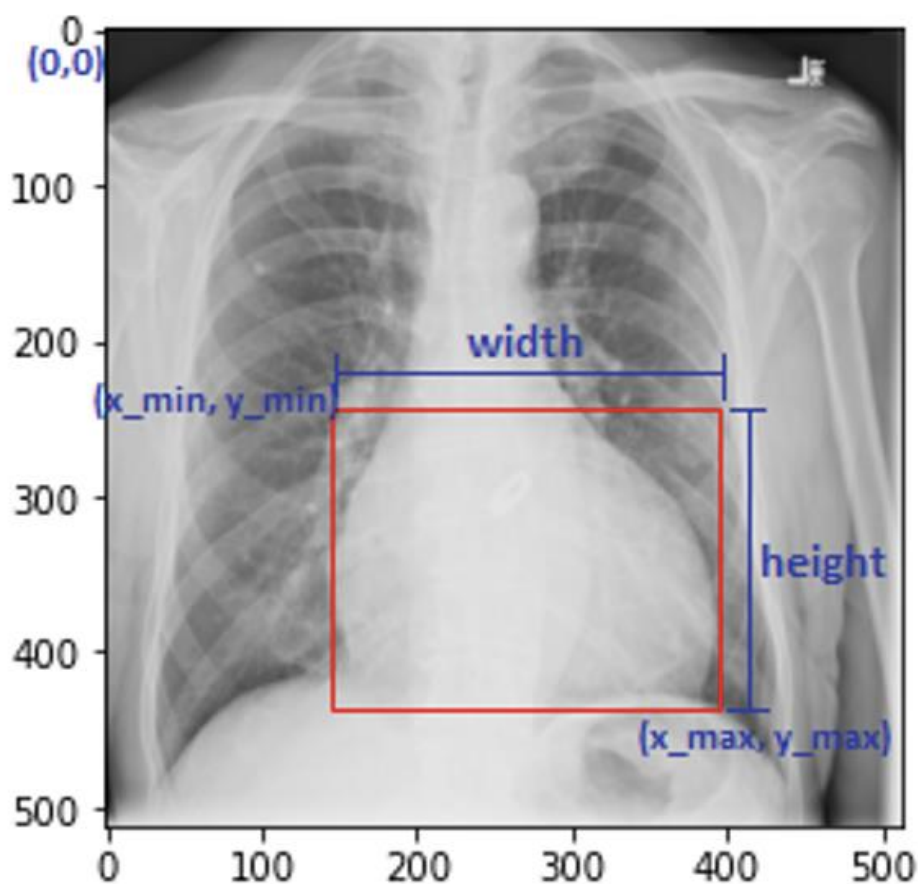
181 **Competing interests:**

182 The authors declare that they have no competing interests.

183

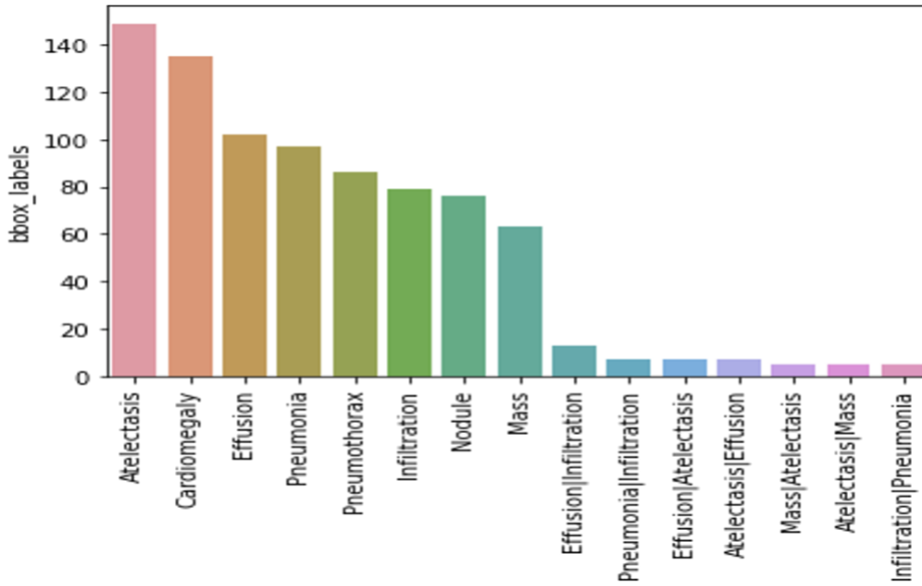
184 **Figures:**

185 **Figure 1: Depicts the location of cardiomegaly with bounding boxes.**



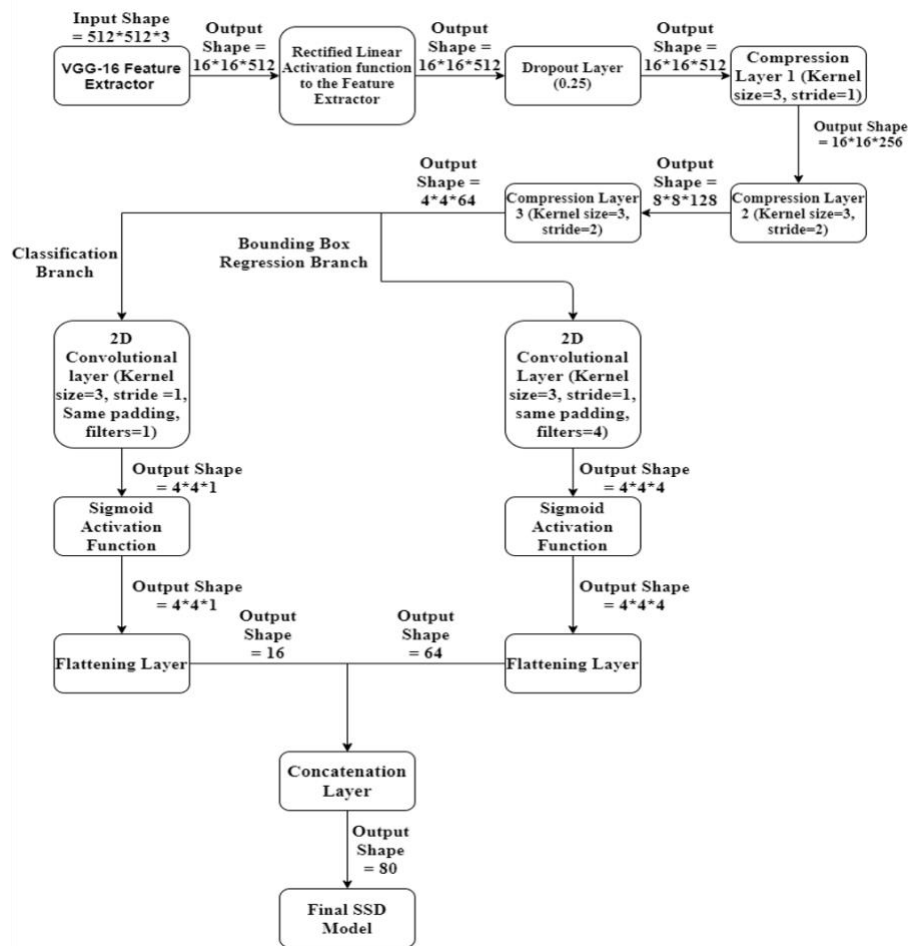
186

187 **Figure 2: The plot for the top 15 labels.**



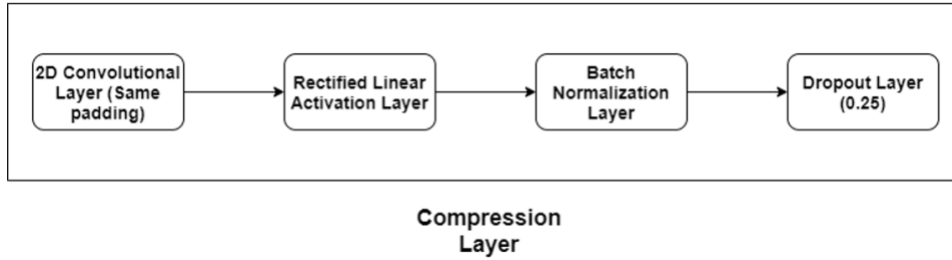
188  
189

Figure 3: The SSD model architecture.



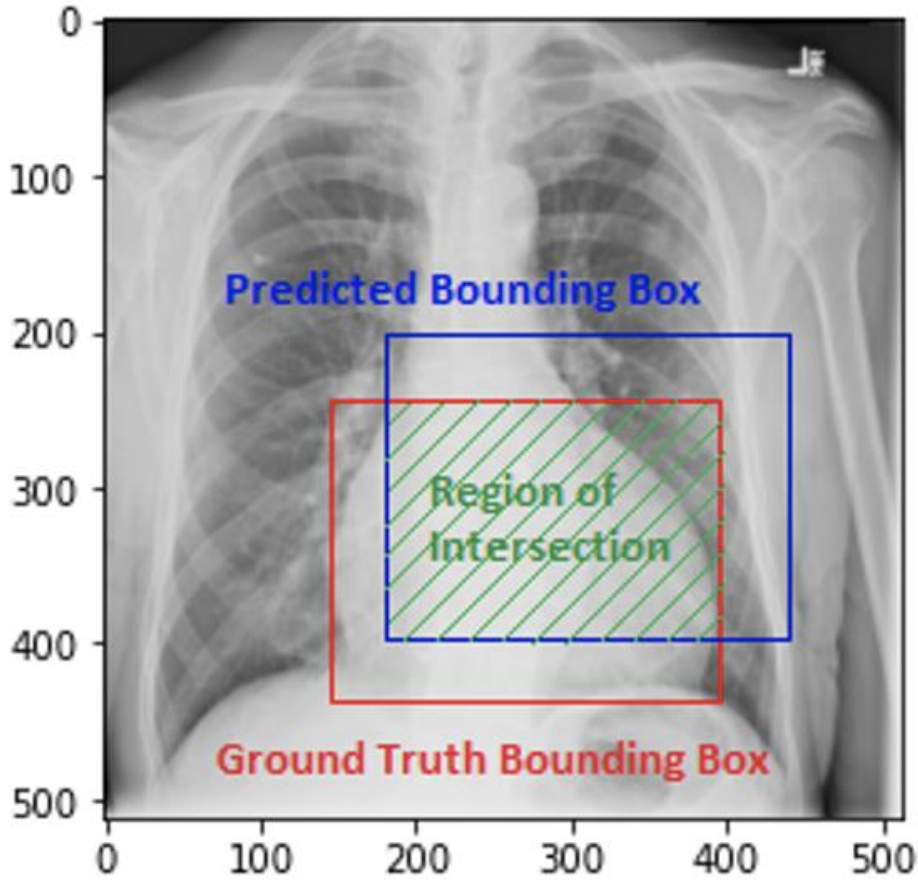
190  
191

Figure 4: Compression layer architecture used in SSD model.



192  
193  
194

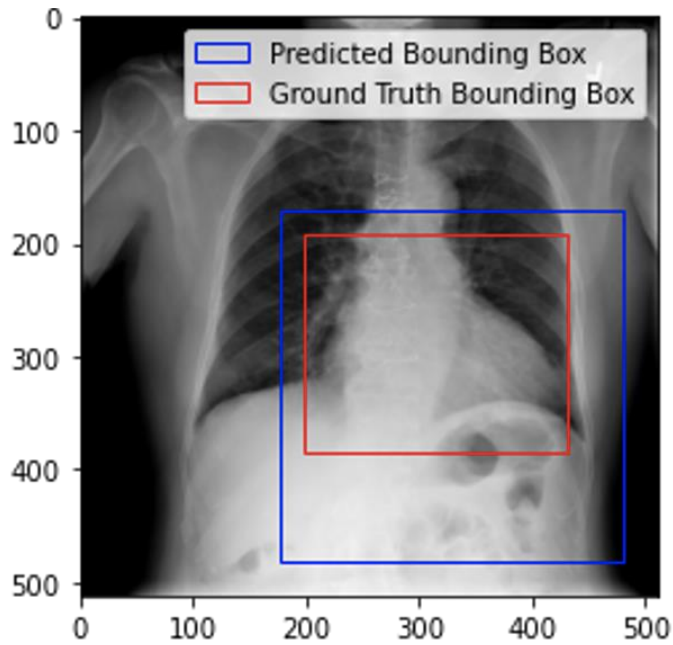
**Figure 5: Image of a patient suffering from cardiomegaly showing intersection over union policy for the custom cost function.**



195  
196  
197

**Figure 6: Comparison of ground truth bounding box with the bounding box predicted with SSD Model.**





198  
199  
200  
201

**Tables:**

**Table 1: Number of training batches, sizes and input pixel resolution for bounding box algorithms.**

Label	No. of Training Examples	Batch Size	Total No. of Batches	Input pixel resolution
Atelectasis	149	4	38	512*512
Cardiomegaly	135	4	34	512*512
Effusion	102	4	26	512*512
Infiltration	79	4	20	512*512
Mass	63	4	16	512*512
Nodule	76	4	19	512*512
Pneumonia	97	4	25	512*512
Pneumothorax	86	4	22	512*512
Secondary Labels	93	-	-	-
Total: 880				

202  
203

**Table 2: Number of training epochs and losses for all algorithms.**

<b>Bounding Box Algorithm</b>	<b>Optimizer Used</b>	<b>Learning Rate</b>	<b>No. of Training Epochs</b>	<b>Initial Loss</b>	<b>Final Loss</b>
<b>Atelectasis</b>	Adam	1e-4	50	11.91	1.23
<b>Cardiomegaly</b>	Adam	1e-2	38	2.95	1.05
<b>Effusion</b>	Adam	1e-3	50	7.85	1.09
<b>Infiltration</b>	Adam	1e-3	50	9.43	0.97
<b>Mass</b>	Adam	1e-3	50	10.64	1.19
<b>Nodule</b>	Adam	1e-3	50	8.24	1.50
<b>Pneumonia</b>	Adam	1e-3	50	7.45	0.89
<b>Pneumothorax</b>	Adam	1e-3	50	8.44	1.00

204

205 **References:**

206

207 1. Ross Girshik, Fast R-CNN, ICCV 2015. arXiv:1504.08083.

208

209 2. Shaoqing Ren, Kaiming He, Ross Girshick, Jian Sun, Faster R-CNN: Towards Real-Time  
210 Object Detection with Region Proposal Networks, Advances in Neural Information Processing  
211 Systems, 2015.

212

213 3. Intel® Integrated Performance Primitives Developer Reference, Histogram of Oriented  
214 Gradients (HOG) Descriptor, retrieved from:  
215 <https://software.intel.com/content/www/us/en/develop/documentation>

216

217 4. Joseph Redmon, Santosh Divvala, Ross Girshick, Ali Farhadi, You Only Look Once: Unified,  
218 Real-Time Object Detection, IEEE, 2016.

219

220 5. Ross Girshick, Jeff Donahue, Trevor Darrell, Jitendra Malik, Rich feature hierarchies for  
221 accurate object detection and semantic segmentation, IEEE, 2014.

222

223 6. Jifeng Dai, Yi Li, Kaiming He, Jian Sun, R-FCN: Object Detection via Region-based Fully  
224 Convolutional Networks, arxiv, 2016.

225

- 226 7. Wei Liu, Dragomir Anguelov, Dumitru Erhan, Christian Szegedy, Scott Reed, Cheng-Yang Fu,  
227 Alexander C. Berg, SSD: Single Shot MultiBox Detector, arxiv, 2016.  
228
- 229 8. Kaiming He, Xiangyu Zhang, Shaoqing Ren, and Jian Sun, Spatial Pyramid Pooling in Deep  
230 Convolutional Networks for Visual Recognition, arxiv, 2016.  
231
- 232 9. Jonathan-hui, Object detection: speed and accuracy comparison (Faster R-CNN, R-FCN, SSD,  
233 FPN, RetinaNet and YOLOv3), retrieved from: <https://jonathan-hui.medium.com/>  
234
- 235 10) Technostacks, YOLO Vs. SSD: Choice of a Precise Object Detection Method, Retrieved from:  
236 <https://technostacks.com/blog/yolo-vs-ssd>